remote sensing

MDPI

Article

Method for Landslide Area Detection with RVI Data Which Indicates Base Soil Areas Changed from Vegetated Areas

Kohei Arai [1,*], Yushin Nakaoka [2] and Hiroshi Okumura [1]

[1] Department of Information Science, Science and Engineering Faculty, Saga University, Saga 840-8502, Japan; okumurah@edu.cc.saga-u.ac.jp
[2] Graduate School of Science and Engineering Faculty, Saga University, Saga 840-8502, Japan; 23726025@edu.cc.saga-u.ac.jp
* Correspondence: arai@is.saga-u.ac.jp

Abstract: This study investigates the use of the radar vegetation index (RVI) derived from Sentinel-1 synthetic aperture radar (SAR) data for landslide detection. Traditional landslide detection methods often rely on the Normalized Difference Vegetation Index (NDVI) derived from optical imagery, which is susceptible to limitations imposed by weather conditions (clouds, rain) and nighttime. In contrast, SAR data, acquired by Sentinel-1, provides all-weather, day-and-night coverage. To leverage this advantage, we propose a novel approach utilizing RVI, a vegetation index calculated from SAR data, to identify non-vegetated areas, which often indicate potential landslide zones. To enhance the accuracy of non-vegetated area classification, we employ the high-performing EfficientNetV2 deep learning model. We evaluated the classification performance of EfficientNetV2 using RVI derived from Sentinel-1 SAR data with VV and VH polarizations. Experiments were conducted on SAR imagery of the Iburi district in Hokkaido, Japan, severely impacted by an earthquake in 2018. Our findings demonstrate that the classification performance using RVI with both VV and VH polarizations significantly surpasses that of using VV and VH polarizations alone. These results highlight the effectiveness of RVI for identifying non-vegetated areas, particularly in landslide detection scenarios. The proposed RVI-based method has broader applications beyond landslide detection, including other disaster area assessments, agricultural field monitoring, and forest inventory.

Keywords: efficientNetV2; radar vegetation index: RVI; sentinel-1/SAR; VV and VH polarization; landslide detection

check for updates

Academic Editors: Xueling Wu, Faming Huang, Diego Di Martire, Marco Mulas and Massimo Conforti

Received: 20 December 2024
Revised: 22 January 2025
Accepted: 7 February 2025
Published: 12 February 2025

Citation: Arai, K.; Nakaoka, Y.; Okumura, H. Method for Landslide Area Detection with RVI Data Which Indicates Base Soil Areas Changed from Vegetated Areas. *Remote Sens.* **2025**, *17*, 628. https://doi.org/10.3390/rs17040628

Copyright: © 2025 by the authors. Licensee MDPI, Basel, Switzerland. This article is an open access article distributed under the terms and conditions of the Creative Commons Attribution (CC BY) license (https://creativecommons.org/licenses/by/4.0/).

1. Introduction

The radar vegetation index (RVI) is a quantitative metric used in remote sensing and agriculture to assess the health and density of vegetation using radar data. The Normalized Difference Vegetation Index (NDVI) is derived from optical sensor onboard satellites and usually used for the detection of vegetated areas and to assess the vitality of the vegetation. Therefore, the NDVI can be obtained with fine weather conditions in daytime. Unlike optical indices, the RVI utilizes synthetic aperture radar (SAR) data, which can penetrate clouds and is unaffected by weather conditions or daylight, making it valuable for continuous monitoring.

According to the Copernicus documentation, the RVI is calculated using the formula:

$$RVI = \frac{4\sigma^0_{VH}}{\sigma^0_{VV} + \sigma^0_{VH}} \quad (1)$$

where σ^0_{VH} and σ^0_{VV} represent the polarimetric backscattering coefficients for cross-polarized (VH) and co-polarized (VV) channels, respectively [1]. There are two orthogonal polarizations, vertical and horizontal, in linear polarization for the radio waves which are used for SAR. VH denotes that the vertical polarization of radio waves is transmitted, and the horizontal polarization of radio waves is received while VV denotes that the vertical polarization of radio waves is transmitted, and the vertical polarization of radio waves is received. These coefficients are derived from the radar signals captured in different polarizations, providing insights into vegetation structure and moisture content.

The RVI has been employed in various studies, including monitoring crop growth stages, assessing vegetation biomass, and analyzing forest canopy structures. The Sentinel-1 Ground Range Detected (GRD) dataset offers accessible SAR data for calculating RVI and analyzing vegetation health over large areas. Additional information and research on RVI can be found on relevant forums [2], the "Radar Vegetation Index for Sentinel-1 (RVI4S1) Script" [3], and the Copernicus Data Space Ecosystem, which provide guidance on calculating the RVI using the Sentinel-1 GRD collection [4].

The application of the RVI in disaster detection and monitoring is proposed in this paper. One significant advantage of SAR data is its ability to be acquired under all weather conditions and during both day and night. This capability makes SAR data particularly useful for detecting and monitoring disasters that occur during adverse weather or darkness—situations where optical sensors are ineffective. Therefore, this paper proposes the utilization of RVI for disaster detection and monitoring, expanding its application beyond traditional agricultural and forestry uses.

There are types of meteorological disasters. Meteorological disasters encompass a wide range of events that can affect vegetation and infrastructure. The main types include:

- Heavy Rain Damage: Caused by heavy or torrential rain, leading to flooding and soil erosion.
- Wind Damage: Resulting from strong winds or tornadoes, damaging vegetation and structures.
- Lightning Damage: Caused by lightning strikes and hail, affecting crops and trees.
- Heavy Snow Damage: Due to significant snowfall in a short period, leading to structural damage and vegetation stress.
- High Tide and Storm Surge Damage: Resulting from rising sea levels and seawater inundation during typhoons or low-pressure systems.
- Flood Damage: Caused by overflowing rivers and water bodies, affecting land and vegetation.
- Drought Damage: Stress on vegetation due to prolonged lack of precipitation.
- Cold and Frost Damage: Occurring during unseasonal low temperatures, affecting crop growth.
- Salt Wind Damage: Damage to plants and infrastructure from salt particles carried inland by strong sea winds.

Additionally, other meteorological disasters include avalanches, snowmelt damage, snow accumulation, dry damage, poor visibility, and recurrent frost damage. The Japan Meteorological Agency issues weather warnings for heavy rain, flooding, high waves, storm surges, heavy snow, windstorms, and blizzards, reflecting the importance of monitoring these events. Meteorological disasters can occur independently or simultaneously. For example, typhoons often bring heavy rain, flooding, high waves, storm surges, and windstorms concurrently.

The detection of disasters can be performed using vegetation indices. Vegetation indices, particularly the Normalized Difference Vegetation Index (NDVI), have been instru-

mental in detecting and assessing certain types of meteorological disasters. The NDVI is sensitive to changes in plant health and can detect:

- Drought Damage: Indicated by a decrease in NDVI due to plant stress from lack of water.
- Cold Damage: Reflected as lower NDVI values due to inhibited plant growth in low temperatures.
- Salt Damage: Observed as reduced NDVI values owing to the detrimental effects of salinity on plants.
- Frost Damage: Detected through changes in NDVI resulting from frost impact on vegetation.

However, the NDVI relies on optical data from satellites, which are often unavailable during cloudy or adverse weather conditions. This limitation hampers continuous monitoring, particularly during disasters when timely data is crucial.

This paper enhances the advantages of the RVI for disaster monitoring. Landslides, slope failures, and other events leading to vegetation loss expose bare ground, making them detectable through changes in vegetation indices. The RVI, derived from SAR data, offers a significant advantage in such scenarios. Its all-weather, day-and-night acquisition capability ensures consistent data availability, enabling the detection and monitoring of disasters even under cloud cover or during nighttime.

This approach to utilizing the RVI in place of the NDVI is a valuable contribution to the field of remote sensing. By integrating the RVI into disaster monitoring systems, more accurate and timely assessments can be conducted, aiding in emergency response and mitigation efforts. Beyond disaster monitoring, the RVI-based method has multiple applications. Broader applications for the RVI include agricultural field monitoring, for example, which typically requires a time-series analysis of the NDVI to track crop development. However, the NDVI data gaps, which are due to cloud covers, can hinder this analysis. The proposed RVI method circumvents this issue by providing consistent data regardless of weather conditions, enabling an uninterrupted time-series analysis crucial for agricultural management.

The following sections discuss related research on the RVI, outlining previous studies and methodologies. Subsequently, we present the proposed method for utilizing the RVI in disaster detection and monitoring. We then detail the software and hardware requirements necessary for implementing this approach. Finally, we conclude with remarks and discussions on the implications of this method for remote sensing and disaster management.

2. Related Research Works

There is a substantial body of literature related to the radar vegetation index (RVI), providing valuable insights into its calculation methods and applications in remote sensing and agriculture. A comprehensive review of the RVI for crop monitoring is presented by Barrett and Petropoulos (2012) [5], offering a detailed description of the concept of RVI, its calculation methodology, and its application in agricultural monitoring. Similarly, Chen et al. (2013) [6] assesses the effectiveness of using RVI to monitor crop growth and yield, demonstrating its potential for agricultural forecasting.

Advancements in crop monitoring using SAR data are further explored by Jones and Kim (2014) [7] who propose a novel approach for utilizing the RVI in this context. The foundational principles and techniques of remote sensing of vegetation, including the RVI, are thoroughly discussed in the seminal work by Smith and Atkinson (2015) [8], providing essential background for understanding modern remote sensing applications. The effects of crop growth variations on the RVI responses and crop height estimation using dynamic monitoring models are investigated by Wang et al. (2016) [9]. Early developments of

the polarimetric radar vegetation index (PRVI) for biomass estimation in desert fringe ecosystems are presented by Li et al. (2011) [10], alongside the introduction of a dual-polarimetric radar vegetation index for crop growth monitoring using Sentinel-1 SAR data by Zhang et al. (2017) [11].

Further research includes the work by Garcia et al. (2018) [12] who propose methods for soil moisture retrieval over croplands using Sentinel-1 SAR data and dual-polarization L-band GRD SAR data. The monitoring of vegetation cover in tropical regions using a SAR-C dual-polarization index, while investigating seasonal and spatial influences, is studied by Hernandez and Lopez (2019) [13]. Additionally, Kumar et al. (2020) [14] introduce dual-polarimetric descriptors from Sentinel-1 GRD SAR data for crop growth assessment, emphasizing the applicability of SAR data in vegetation monitoring.

Innovative approaches in data processing for RVI are provided by Peterson and Moore (2021) [15], who offer a Python and R blend for processing Sentinel-1 images, extracting SAR-based vegetation indices, and sampling raster data. The potential of Sentinel-1 interferometric coherence as a vegetation index for agriculture is investigated by Davies et al. (2021) [16], highlighting another avenue for utilizing SAR data in agricultural monitoring. Comprehensive methodologies for forest monitoring and biomass estimation are proposed and validated by Nguyen et al. (2022) [17], while Osei et al. (2023) [10] examine the application of PRVI for biomass estimation in agricultural fields. These references collectively provide detailed information on RVI, its calculation methods, and its diverse applications in remote sensing and agriculture, underscoring its significance in vegetation monitoring and assessment.

As for remote sensing-based disaster detection, there are the following papers. In the context of detecting landslides, slope failures, and other disasters that result in vegetation loss and expose bare land, satellite remote sensing has proven invaluable. A comprehensive review by Zhou et al. (2014) [18] summarizes landslide mapping and monitoring techniques using satellite remote sensing technology, introducing applications of optical data, synthetic aperture radar (SAR), and interferometry. Similarly, Martha et al. (2015) [19] review the latest methods and technologies for landslide detection using satellite remote sensing data, comparing optical and radar methods, and discussing their respective advantages and limitations.

Methods for monitoring landslide displacements using satellite SAR interferometry (InSAR) are proposed by Ferretti et al. (2016) [20], demonstrating the capability to detect ground deformation with high temporal and spatial resolution. The integration of deep learning in landslide susceptibility mapping is explored by Youssef et al. (2017) [21], highlighting how combining satellite data with deep learning models enhances the accuracy of landslide detection. An automatic landslide detection method utilizing object-oriented image analysis on high-resolution optical satellite images is presented by Lu et al. (2018) [22], enabling rapid mapping of landslide spatial distribution. Furthermore, Singh et al. (2019) [23] proposes a methodology for landslide mapping and monitoring by combining InSAR and optical remote sensing data, aiming to improve detection accuracy through multi-source data integration.

A case study of landslide detection in the Italian Eastern Alps using Sentinel-1 SAR data are reported by Bovenga et al. (2020) [24], illustrating how frequent data acquisition facilitates the monitoring of landslide activity. Global analyses of fatal landslide occurrences from 2004 to 2016, conducted by Froude and Petley (2021) [25], reveal spatial and temporal patterns of landslide hazards based on satellite data. Additionally, Park et al. (2022) [26] propose a landslide detection method that leverages the Google Earth Engine platform and Sentinel-2 data, utilizing the platform's data processing capabilities for efficient large-area analysis. Comprehensive reviews of remote sensing-based landslide detection methods

using optical and radar satellite data are provided by Chen et al. (2023) [27], summarizing the advantages, limitations, and application examples of various methods. These references offer detailed information on techniques for detecting vegetation loss due to disasters using satellite data, emphasizing the potential of integrating the RVI and other indices in disaster monitoring and assessment.

3. Research Background

At 3:07 a.m. on 6 September 2018, a magnitude 6.7 earthquake struck the central-eastern Iburi region of Hokkaido. The earthquake recorded a maximum seismic intensity of 7 in Atsuma Town, marking the first time in Hokkaido's history that such a level was reached. The Japan Meteorological Agency officially named it the "2018 Hokkaido Eastern Iburi Earthquake". This earthquake caused widespread slope collapses around the epicenter and triggered liquefaction in Sapporo City, where a seismic intensity of 6-low was observed. These phenomena resulted in significant damage to homes and roads. Tragically, 44 lives were lost, and numerous houses were destroyed, leading to severe impacts across the prefecture. Additionally, the earthquake caused multiple power plant shutdowns, leading to large-scale power outages throughout Hokkaido.

Figure 1 highlights the landslide disasters caused by the earthquake and includes a Google map showing the intensive study area. Detecting these landslides is crucial and can be achieved using the radar vegetation index (RVI) derived from Sentinel-1 SAR data.



(**a**)



(**b**)

Figure 1. Photo of the landslides due to Iburi earthquake which occurred in central Hokkaido, Japan at 3:07 a.m. on 6 September 2018. (**a**) Photo of landslide disasters (https://www.jma-net.go.jp/sapporo/jishin/iburi_tobu.html, accessed on 15 January 2025); (**b**) Google map of the intensive study area.

4. Proposed Method

4.1. Process Flow

Process flow of the proposed flow is shown in Figure 2. To analyze the disaster, Sentinel-1 SAR data acquired before and after the event are first prepared. Speckle noise reduction is performed to enhance classification performance. Next, geometric correction is applied to align the data with topographic maps as the SAR imagery may be distorted due to radar shadowing, foreshortening, and layover. QGIS is used for disaster mapping during this process. The radar vegetation index (RVI) is calculated using Equation (1). The processed SAR data are then divided into 256 × 256-pixel patches to facilitate training, validation, and testing of the learning model, which is based on the EfficientNetV2 architecture. Once the model is trained, validated, and tested, its classification performance is evaluated.

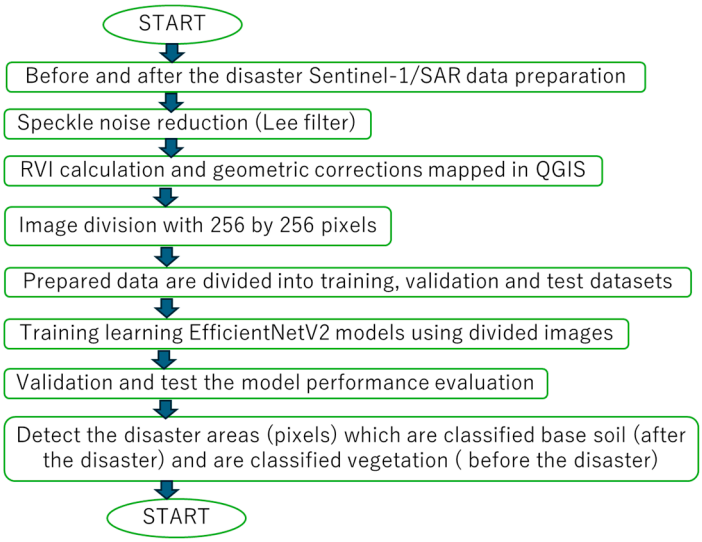


Figure 2. Process flow of the proposed method.

This workflow enables the detection of disaster-affected areas. Specifically, it identifies pixels classified as "bare soil (post-disaster)" that were previously classified as "vegetation (pre-disaster)". This classification is key for detecting landslide-affected regions, as landslides typically result in vegetation being replaced by bare soil.

4.2. Details of the Proposed Method (Classification Method)

Landslides, steep slope collapses, mountainside collapses, and landslides due to earthquakes, which are disasters in which vegetation is lost, and bare ground is left, are detected. Therefore, it is to classify bare ground areas and vegetated areas from the RVI of intensive study area. To classify these areas, the well-known classification method of EfficientNetV2 is used.

EfficientNetV2 shows superior performance compared to the following models:

(i) EfficientNet-B7: EfficientNetV2-M achieves the same accuracy with 11× faster training speed.
(ii) RegNet and ResNeSt: EfficientNetV2 significantly outperforms them in both accuracy and inference speed.
(iii) LambdaNet and NFNet: EfficientNetV2 outperforms them in terms of training time vs. classification accuracy.
(iv) Performance on ImageNet-1K and ImageNet-22K.

In comparison for ConvNeXt, EfficientNetV2 achieves higher accuracy than ViT and Swin-Transformer on both ImageNet-1K and ImageNet-22K4. These results prove that EfficientNetV2 has high classification accuracy compared to other classification methods.

Considering the efficiency and training speed of the model, EfficientNetV2 is one of the best image classification models currently available.

EfficientNetV2 is a family of convolutional neural networks (CNNs) designed for image classification tasks and is known for achieving state-of-the-art accuracy while being computationally efficient. Introduced by Google researchers in 2021, EfficientNetV2 builds upon the original EfficientNet architecture by incorporating several advancements that enhance both accuracy and efficiency compared to other models. Here is an overview of why EfficientNetV2 demonstrates the most accurate classification method compared to other networks:

Optimized Architecture Through Neural Architecture Search (NAS): Training-Aware NAS: EfficientNetV2 utilizes a training-aware neural architecture search that not only focuses on the accuracy of the model but also considers the training speed. This results in architectures that are optimized for faster training without compromising on performance.

Fused MBConv Layers: The introduction of fused mobile inverted bottleneck convolution (MBConv) layers improves the model's ability to capture features efficiently, leading to higher accuracy.

Compound Scaling Approach: Unified Scaling of Dimensions: Similarly to the original EfficientNet, EfficientNetV2 employs a compound scaling method that uniformly scales the network's depth, width, and resolution. This balanced scaling ensures that the model grows in a way that maintains efficiency while improving performance.

Improved Scaling Techniques: EfficientNetV2 refines the scaling strategy to better suit the newer architecture, leading to models that are more accurate at various sizes.

Progressive Learning Method: Adaptive Training Strategy: EfficientNetV2 introduces a progressive learning technique where the model is trained on smaller images initially and gradually transitions to larger images. This approach speeds up training and acts as a form of regularization, enhancing the model's generalization capabilities.

Efficiency in Training: By starting with lower-resolution images, the model converges faster, reducing the overall training time compared to training solely on high-resolution images.

Enhanced Regularization Techniques: Improved Regularization Methods: The model incorporates advanced regularization techniques such as RandAugment (an automated data augmentation strategy) and stochastic depth, which help prevent overfitting and improve accuracy.

Label Smoothing and Dropout: These additional regularization methods further enhance the model's robustness and ability to generalize from training data.

Performance on Benchmark Datasets: State-of-the-Art Results on ImageNet: EfficientNetV2 achieves top-tier accuracy on ImageNet, a large-scale dataset widely used for benchmarking image classification models. It surpasses previous models in both accuracy and efficiency.

Comparison with Other Models: When compared to models like ResNets, Vision Transformers (ViT), and other EfficientNets, EfficientNetV2 offers superior accuracy with reduced computational requirements.

Model Efficiency: Faster Inference Times: EfficientNetV2 models are designed to be computationally efficient, resulting in faster inference times which are critical for real-world applications where latency matters.

Resource Utilization: The models require fewer parameters and FLOPS (floating-point operations per second) to achieve high accuracy, making them suitable for deployment of devices with limited resources.

Advancements Over Previous Models: Comparison with EfficientNet: While the original EfficientNet models were already efficient, EfficientNetV2 brings improvements in training speed and scaling, leading to even better performance.

Edge Over Vision Transformers: Although Vision Transformers have shown impressive results, they often require large amounts of data and computational resources. EfficientNetV2 achieves comparable or better accuracy with less computational overhead.

In summary, EfficientNetV2 stands out as one of the most accurate classification methods due to its optimized architecture, efficient scaling, progressive learning strategies, and state-of-the-art performance on benchmark datasets. Its ability to achieve high accuracy without excessive computational demands makes it preferable over other methods, especially in environments where resources and training time are constrained. By addressing both the model's architecture and training procedures, EfficientNetV2 effectively balances the trade-offs between accuracy, efficiency, and resource utilization, setting a new standard for image classification models up to the cutoff in October 2023.

PyTorch 2.0 is an open-source deep learning framework developed by Facebook, and its flexibility and ease of use have made it popular with many researchers and developers. In particular, the use of dynamic computation graphs makes it easier to debug and modify code. This allows for the rapid iteration of experiments and rapid validation of new ideas. On the other hand, EfficientNetV2 is an image classification model developed by Google that combines high accuracy and efficiency. By optimizing the model scaling strategy, EfficientNetV2 achieves high performance while using computational resources efficiently. This combination makes it possible to build an efficient and powerful image classification model. PyTorch allows to intuitively and efficiently build, train, and debug models using the natural Python code style. One of the key features of PyTorch is the dynamic computation graph, which allows the computation graph to be dynamically constructed at runtime, enabling more flexible model construction. PyTorch also provides many pre-trained models, allowing users to quickly start their projects.

EfficientNetV2 is a new computer vision model designed based on the theory of model scaling. Compared with traditional EfficientNet, EfficientNetV2 provides higher accuracy and efficiency. Its main advantages include efficient use of computational resources, high performance, and reduced model size. This allows EfficientNetV2 to achieve high accuracy even in resource-limited environments. Therefore, we decided to use a method that combines Pytorch and EfficientNetV2. The combination of PyTorch and EfficientNetV2 offers both flexibility and efficiency. PyTorch's dynamic graph, combined with EfficientNetV2's highly optimized model scaling strategy, can significantly improve the speed and accuracy of research and development. This combination allows us to build highly accurate image classification models with fewer computational resources, enabling rapid prototyping and experimentation.

The balance of a dataset has a significant impact on the fairness and performance of a model. An imbalanced dataset can cause model bias. To solve this problem, data resampling and adjusting class weights are effective. In PyTorch, it can be use 'WeightedRandomSampler' to balance the data. EfficientNetV2 allows to tune the behavior and performance of the model through configuration settings, from basic configuration settings to customized architecture settings, allowing them to build models that are optimal for specific tasks and datasets. Basic configuration settings for EfficientNetV2 include model type, input size, batch size, number of epochs, etc. These settings directly affect the model performance and training efficiency.

Tuning hyperparameters is important to optimize model performance: by adjusting the learning rate, batch size, number of epochs, dropout rate, etc., it can be possible to improve the accuracy of our model. We optimized the hyperparameters using the PyTorch optimizer. Also, the architecture of EfficientNetV2 can be customized to suit specific needs: for example, it can change the final layer to adjust the number of classes or add

intermediate layers to emphasize specific features. We customized the architecture by instantiating the model.

Saving and managing configuration settings is important for model reproducibility and production management. PyTorch allows us to save configuration in the form of a dictionary and reload it later. Optimizing a model for production requires tuning configuration settings, which are important for optimizing inference speed and memory usage, such as adjusting batch size and scheduling learning rate. When building an image classification model, it needs to define various functions, such as defining a data loader, building a model, selecting a loss function and optimization method, implementing a training loop, and defining an evaluation function. Proper implementation of these functions can efficiently manage the model's learning process. A data loader is responsible for generating mini batches from a dataset and feeding them to the model. The PyTorch 'DataLoader' class makes it easy to define a data loader.

Model construction is performed by defining and ordering layers. When using EfficientNetV2, it can be possible to base our model on a pre-trained model and customize the final layer. Model construction is performed by defining and ordering layers. When using EfficientNetV2, we use a pre-trained model as a base and customize the final layer. This is performed by instantiating the model with efficientnet_pytorch. A loss function is used to measure the error between the model's predictions and the actual labels. Optimization techniques provide a parameter update method to minimize this error. Here, we decided to use cross-entropy loss and the SGD optimizer. The training loop trains the model every epoch, calculates the loss and updates the parameters. It is also important to evaluate the model's performance using a validation dataset.

An evaluation function is used to quantify the predictive performance of a model. Commonly used metrics include accuracy, precision, recall, and F1 score. Here, we define the evaluation function (accuracy, precision, recall, AUC, ROC curve, confusion matrix, and F1 score) for the model and perform the evaluation.

5. Experiment

5.1. Data Used

The training data were sourced from Sentinel-1 SAR VV and VH polarization datasets acquired on 20 August, 24 August, 13 September, and 17 September 2018. These dates correspond to pre-disaster and post-disaster periods. The data processing involved the following steps:

(1) Noise Removal and Calibration: Speckle noise was removed using the Lee filter, followed by calibration to enhance data quality.
(2) Geometric Correction: Range Doppler Terrain Correction was applied to address distortions and align the data with geographic coordinates.
(3) RVI Calculation: The radar vegetation index (RVI) was computed using the formula (Equation (1)). RVI = 4·VH/(VV + VH) in QGIS. The processed RVI data was exported from the overlapping area for further analysis.
(4) Resolution Adjustment: Due to resolution expansion during processing, the data no longer maintained the original 10 m per pixel resolution.
(5) Data Division: The processed data were divided into 256 × 256-pixel patches for each of the following datasets: RGB, RVI, VV, and VH. To ensure consistency, the image names across all folders were standardized.
(6) Data Classification and Labeling: Post-Disaster Data (13 and 17 September 2018): RGB data were classified into three categories: disaster areas, non-disaster areas, and unclassified areas (where disaster presence was indeterminate)

Based on this classification, corresponding RVI, VV, and VH data were labeled and categorized accordingly. Pre-disaster data (20 and 24 August 2018): All data from these dates were labeled as non-disaster since they were acquired before the earthquake.

The data were divided into training, validation, and testing sets:

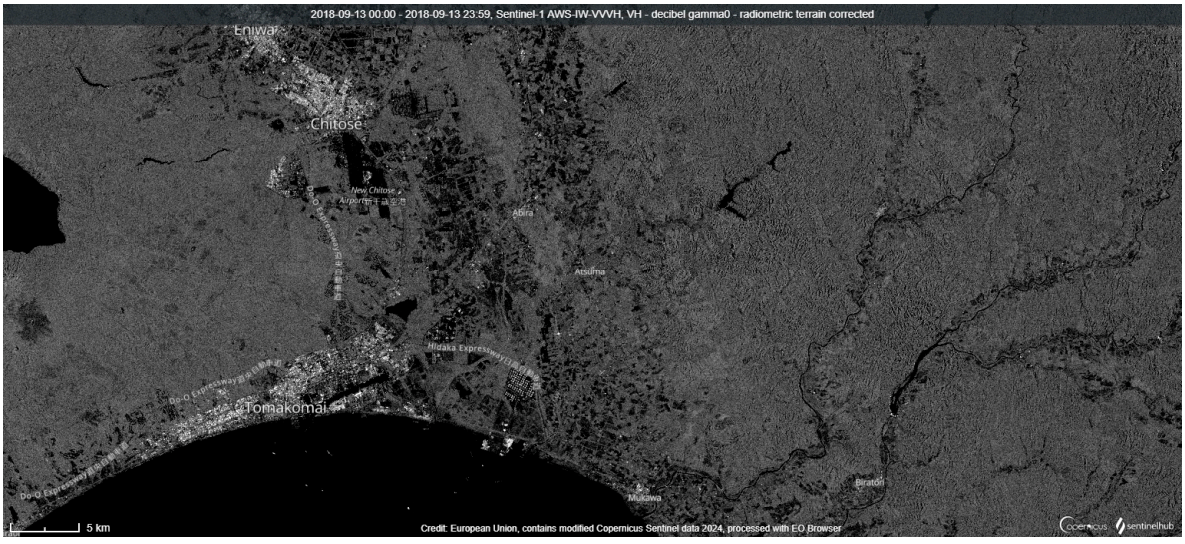
(1) Training Set: Disaster data: 96 samples (augmented 4× Via rotation), Non-disaster data: 146 samples
(2) Validation Set: Disaster data: 32 samples, Non-disaster data: 50 samples
(3) Testing Set: Disaster data: 32 samples, Non-disaster data: 50 samples

Since disaster-related data were limited, it was augmented by applying rotations, effectively increasing the dataset size fourfold.

Figure 3 illustrates the VV and VH polarization data from Sentinel-1 SAR of Atsuma, Hokkaido, acquired on 13 September 2018 (post-earthquake) and 1 September 2018 (pre-earthquake). These datasets were used in experiments to detect disaster-affected areas.

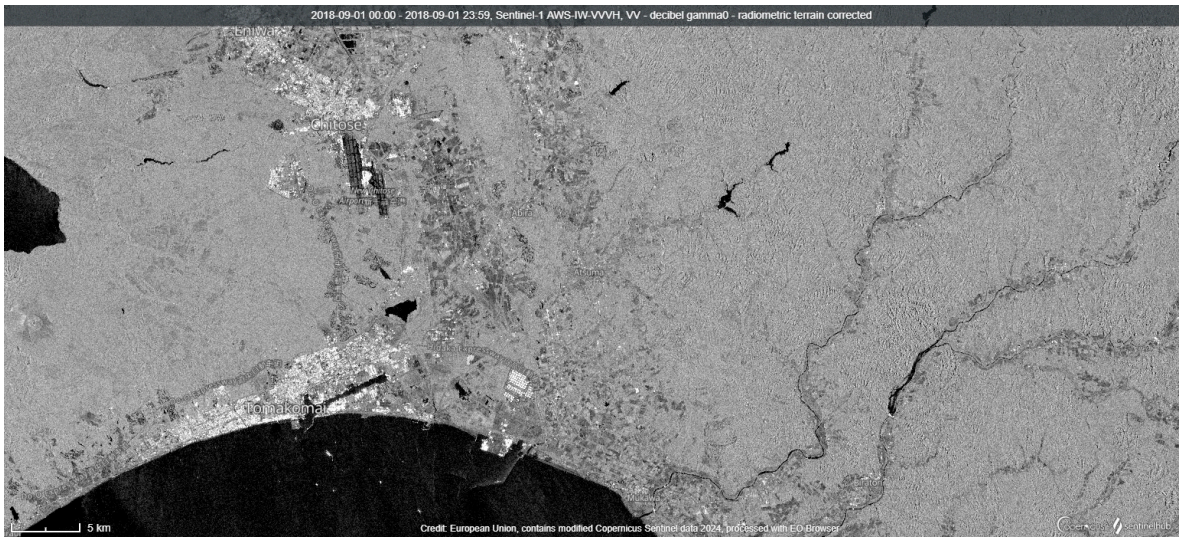
The analyzed results of VV and VH polarization changes in the Iburi, Atsuma area are as follows: The backscatter signals from Sentinel-1 SAR data reveal significant changes in the Iburi, Atsuma area due to the earthquake:

(1) VH Polarization (Single/Odd Scattering): The VH polarization backscatter signals increased after the earthquake, as observed by comparing Figure 3a,c. This increase is attributed to the land cover change from vegetation to bare ground, resulting in higher single scattering.
(2) VV Polarization (Double/Even Scattering): In contrast, VV polarization backscatter signals decreased after the earthquake. This reduction is due to the removal of vegetation and the exposure of bare ground, which diminishes double scattering interactions.
(3) Incidence Angle Dependency: Both VV and VH polarizations exhibit incidence angle dependency. This behavior arises from differences in single and multiple scattering mechanisms during the interaction of the target surface with the electromagnetic waves. These distinctions allow VV and VH polarizations to be effectively differentiated based on their angle-dependent scattering characteristics.

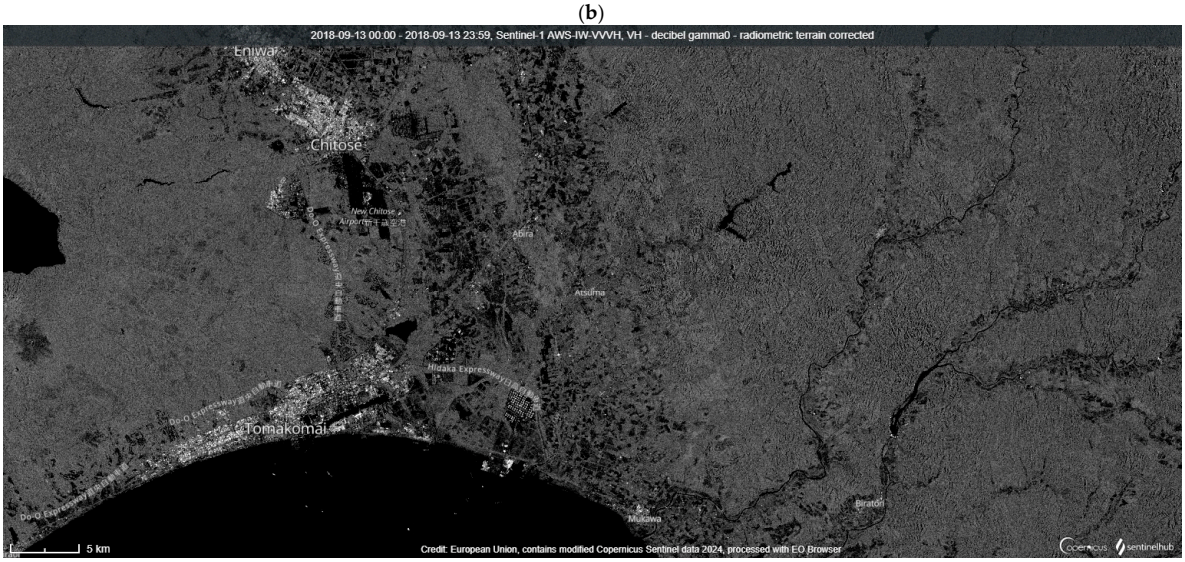


(**a**)

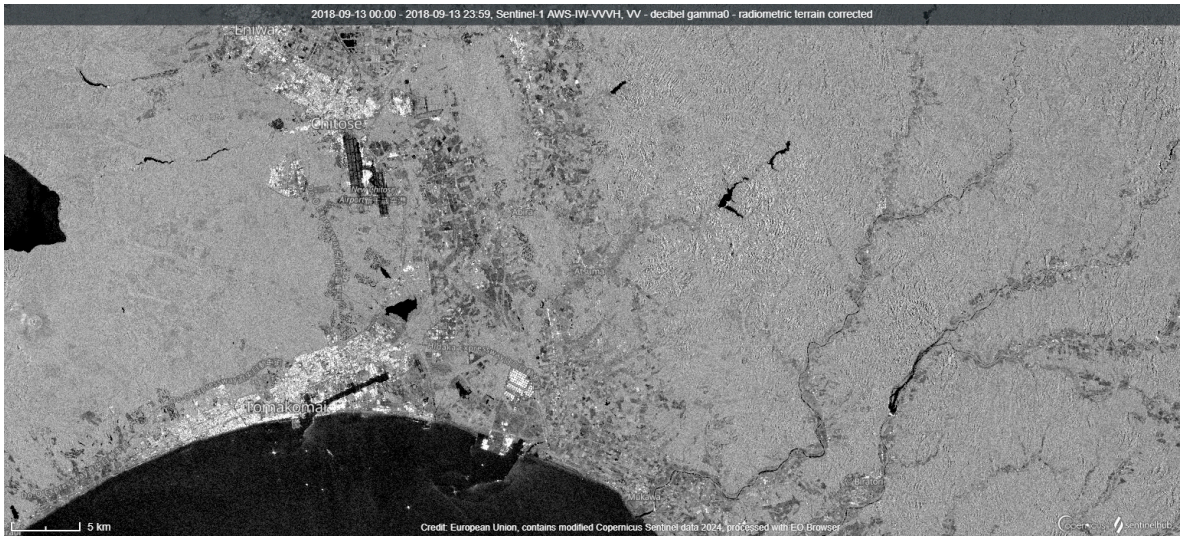
Figure 3. *Cont.*



(**b**)



(**c**)

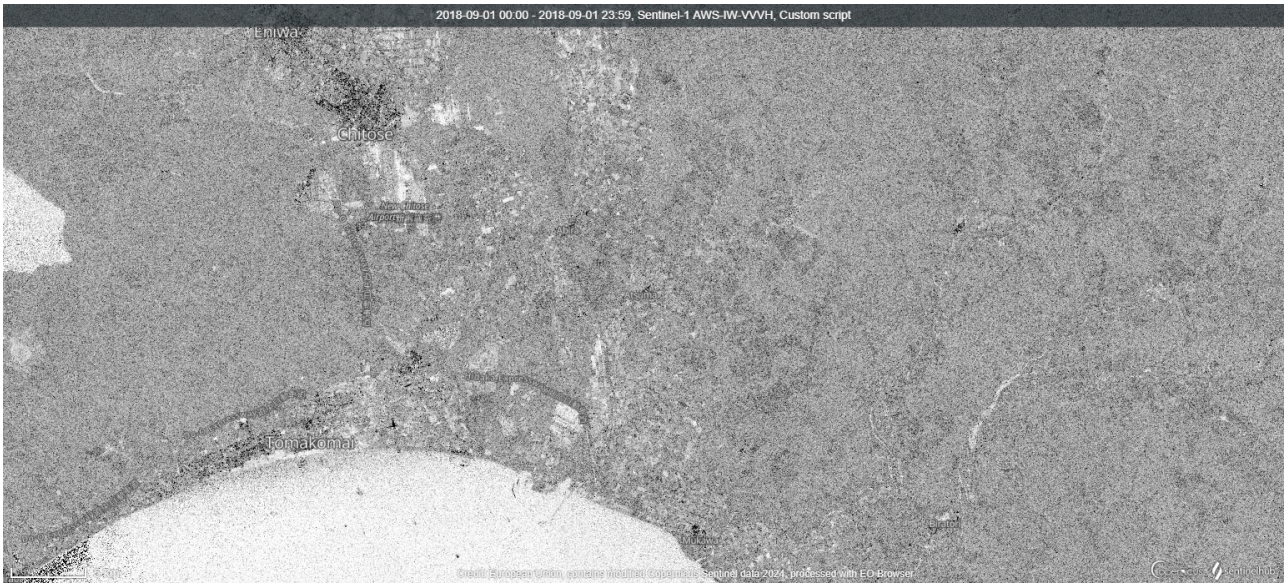


(**d**)

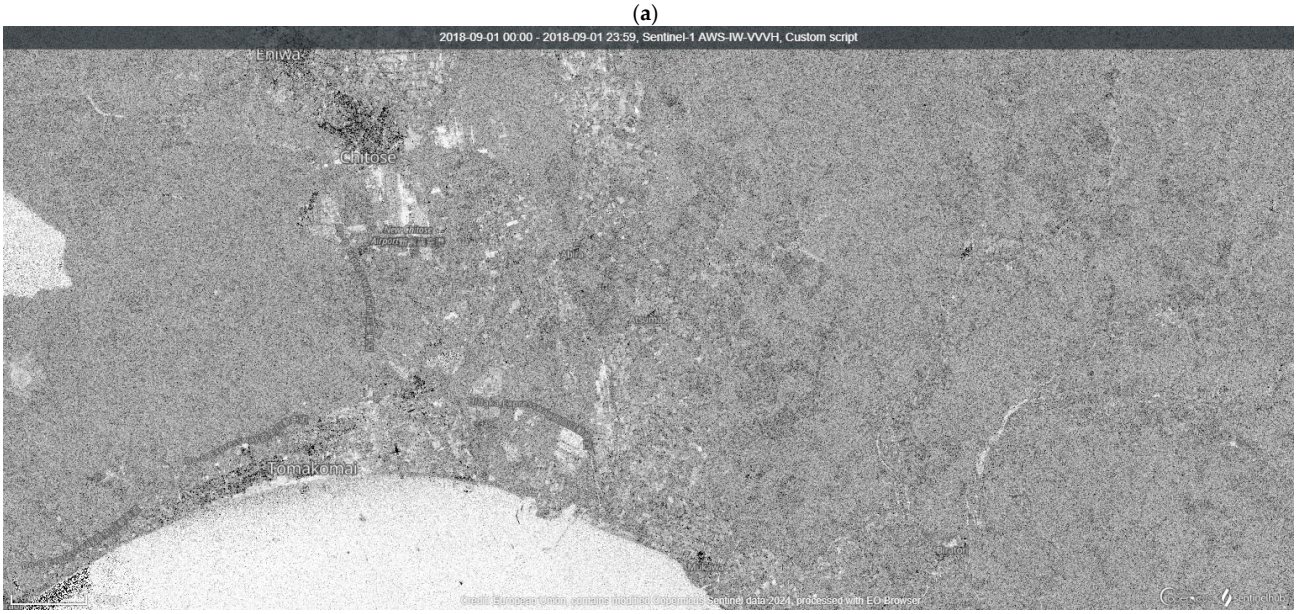
Figure 3. VV and VH polarization data of Sentinel-1/SAR data of Atsuma, Hokkaido acquired on 13 September 2018 (After earthquake) and 1 September 2018 (before earthquake). (**a**) VH polarization, 13 September 2018; (**b**) VV polarization, 13 September 2018; (**c**) VH polarization, 1 September 2018; (**d**) VH polarization, 1 September 2018.

5.2. RVI Calculated

The analyzed results of the RVI changes before and after the earthquake are as follows: Figure 4 presents the radar vegetation index (RVI) calculated using VV and VH polarization backscatter signals based on Equation (1) for the Iburi, Atsuma area in Hokkaido. The data were acquired on two dates: (a) 13 September 2018 (post-earthquake), (b) 1 September 2018 (pre-earthquake). The RVI on 13 September 2018 is noticeably lower than that on 1 September 2018. This decrease in the RVI is attributed to the removal of vegetation caused by the earthquake, as bare ground replaced vegetated areas in the affected region. On the other hand, Figure 4 shows that RVI calculated with the VV and VH polarization of back scatter signals based on Equation (1) of Iburi, Atsuma in Hokkaido acquired on 13 September 2018 (a) and on 1 September 2018 (b), respectively. It is clear that the RVI on 13 September 2018 is lower than that on 1 September 2018 because vegetation has been removed due to the earthquake in the RVI on 13 September 2018.



(**a**)



(**b**)

Figure 4. The RVI calculated with the VV and VH polarization of backscatter signals based on Equation (1) of Iburi, Atsuma in Hokkaido acquired on (**a**) 13 September 2018 and on (**b**) 1 September 2018.

The RVI imagery data for training, validation, and testing are visualized as follows. Figure 5 illustrates samples of RVI imagery data categorized into landslide and non-landslide areas:

(1) Training Samples: (a): Landslide areas, (b): Non-landslide areas
(2) Validation Samples: (c): Landslide areas, (d): Non-landslide areas
(3) Test Samples: (e): Landslide areas, (f): Non-landslide areas

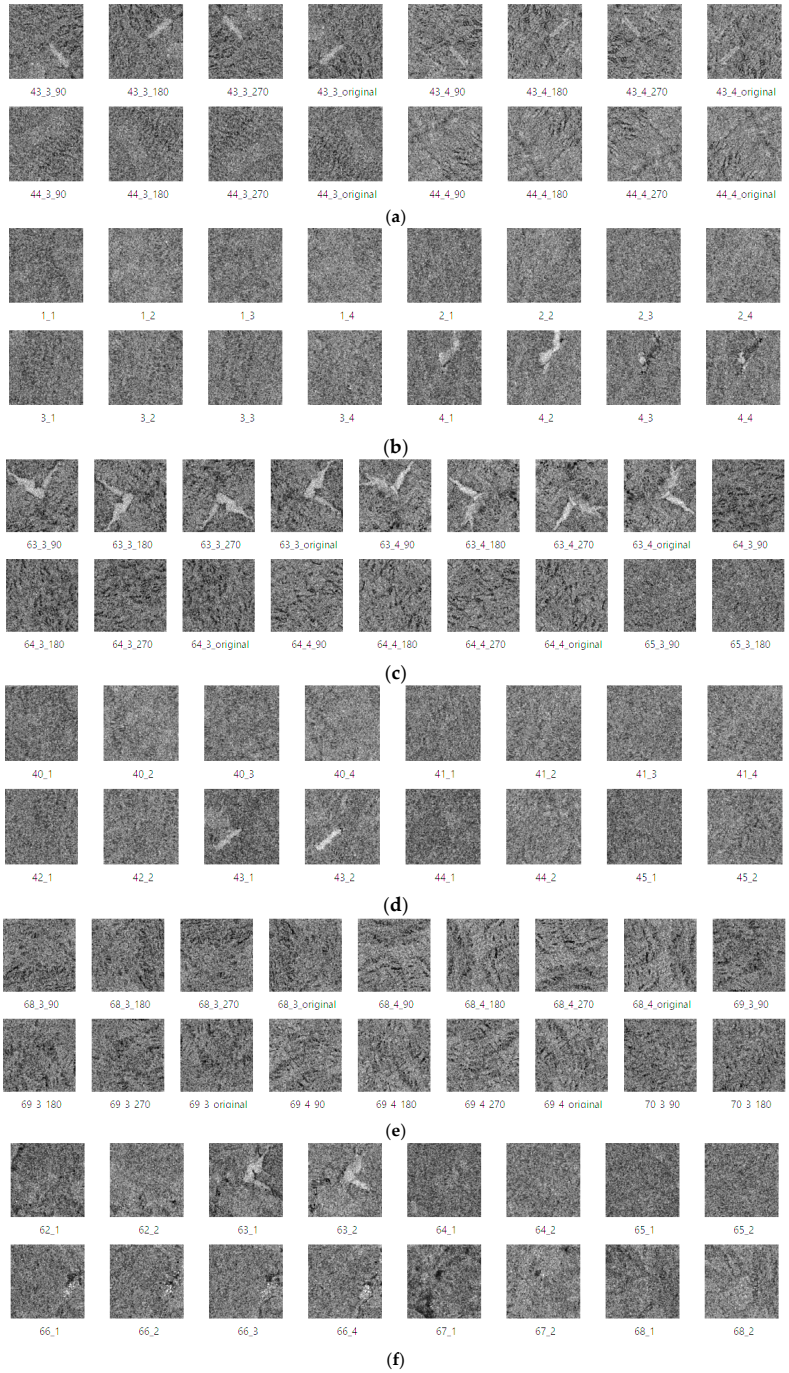


Figure 5. Small portions of training, validation, and test samples of RVI imagery data for landslide areas and those for non-landslide areas. (**a**) A small portion of training samples of RVI imagery data for landslide areas; (**b**) a small portion of training samples of the RVI imagery data for non-landslide areas; (**c**) a small portion of validation samples of the RVI imagery data for landslide areas; (**d**) a small portion of validation samples of the RVI imagery data for non-landslide areas; (**e**) a small portion of test samples of the RVI imagery data for landslide areas; (**f**) a small portion of test samples of the RVI imagery data for non-landslide areas.

Each subfigure provides a representative portion of the dataset used for training, validation, and testing phases in the analysis of landslide detection using RVI imagery data.

VH polarization imagery data for training, validation, and testing are visualized as follows. Figure 6 presents samples of VH polarization imagery data categorized into landslide and non-landslide areas:

(1) Training Samples: (a): Landslide areas, (b): Non-landslide areas
(2) Validation Samples: (c): Landslide areas, (d): Non-landslide areas
(3) Test Samples: (e): Landslide areas, (f): Non-landslide areas

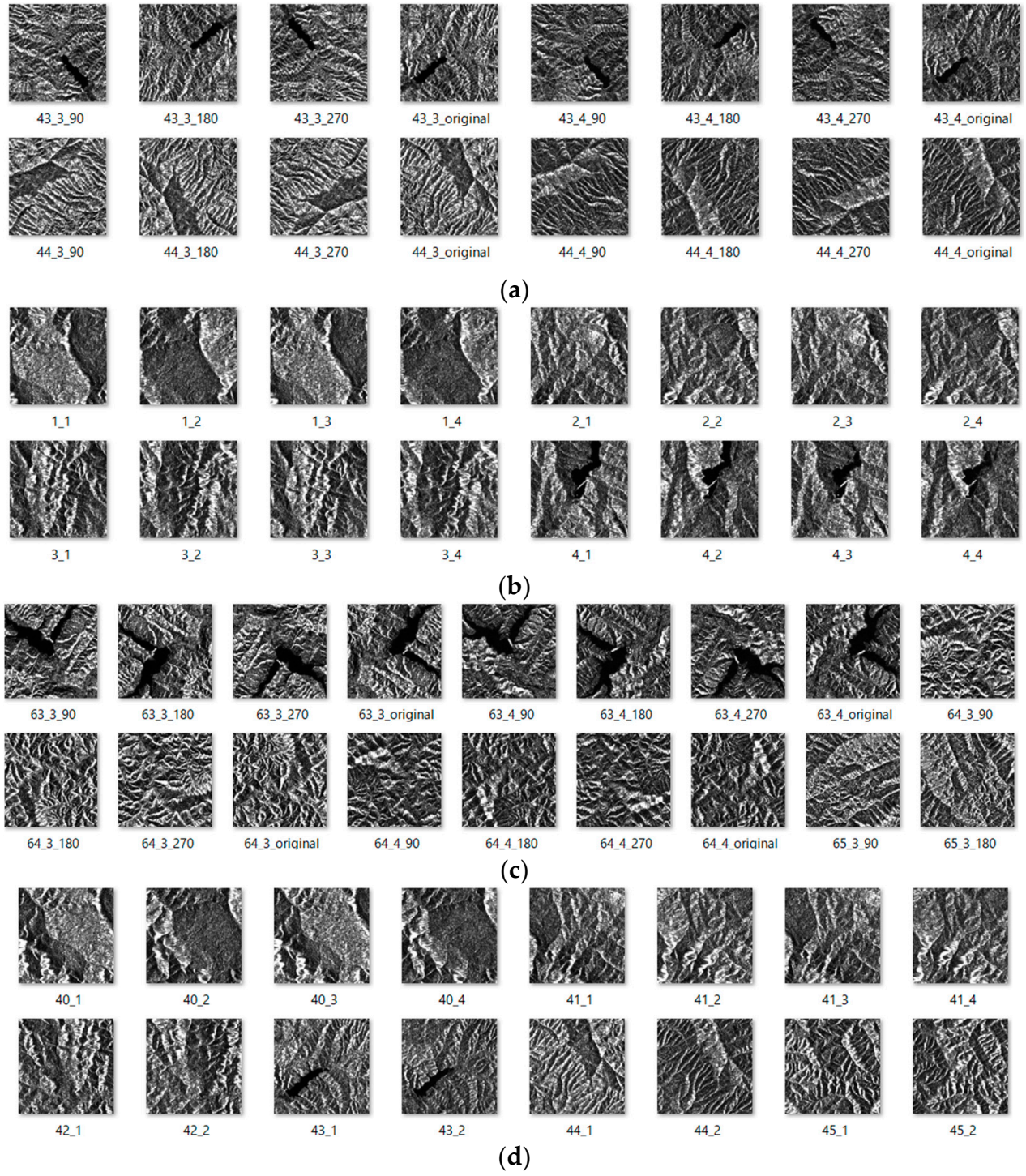


Figure 6. *Cont.*

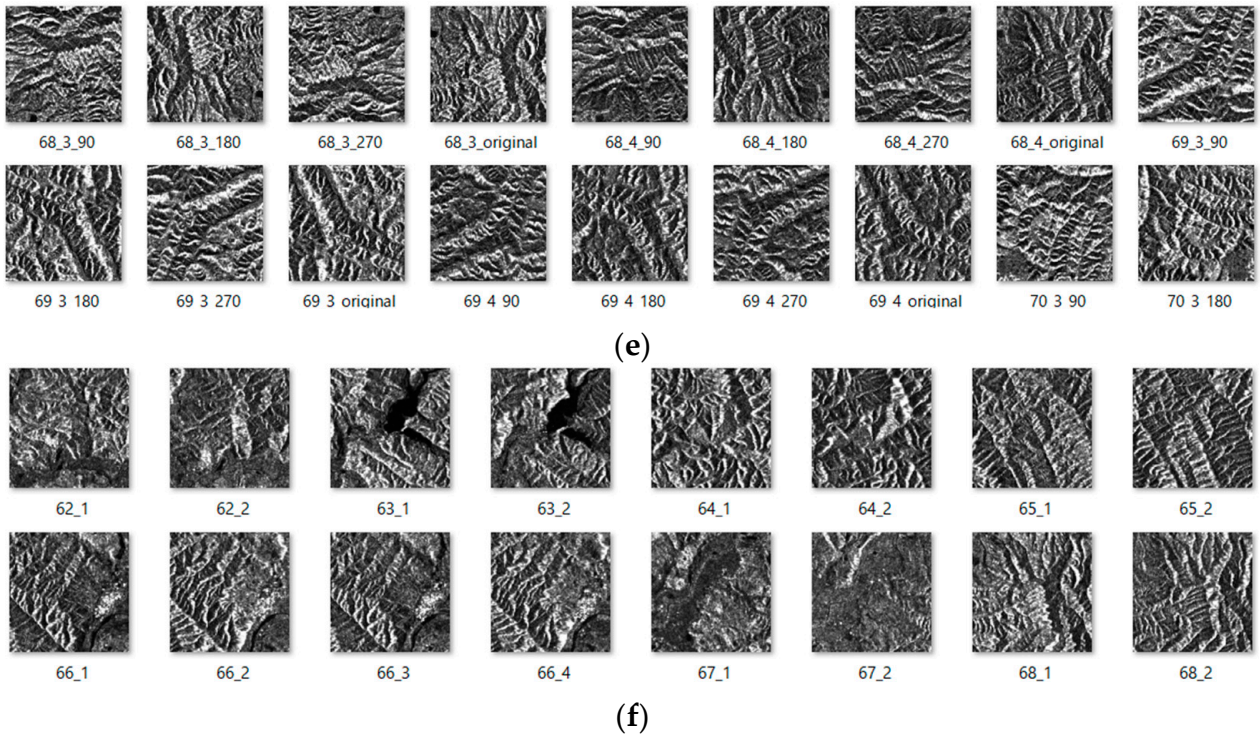


Figure 6. Small portions of training, validation, and test samples of the VH polarization of the imagery data for landslide areas and those for non-landslide areas. (**a**) A small portion of training samples from the VH polarization of the imagery data for landslide areas; (**b**) a small portion of training samples from the VH polarization of the imagery data for non-landslide areas; (**c**) a small portion of validation samples from the VH polarization of the imagery data for landslide areas; (**d**) a small portion of validation samples from the VH polarization of the imagery data for non-landslide areas; (**e**) a small portion of test samples from the VH polarization of the imagery data for landslide areas; (**f**) a small portion of test samples from the VH polarization of the imagery data for non-landslide areas.

Each subfigure provides representative portions of the VH polarization data used during the training, validation, and testing phases for landslide detection.

VV polarization imagery data for training, validation, and testing are visualized as follows. Figure 7 displays samples of VV polarization imagery data categorized into landslide and non-landslide areas:

(1) Training Samples: (a): Landslide areas, (b): Non-landslide areas
(2) Validation Samples: (c): Landslide areas, (d): Non-landslide areas
(3) Test Samples: (e): Landslide areas, (f): Non-landslide areas

These subfigures illustrate representative portions of the VV polarization data used during the training, validation, and testing phases for landslide detection analysis. Figure 7a shows a portion of the training samples of the VV polarization of the imagery data for landslide areas while Figure 7b shows that for non-landslide areas.

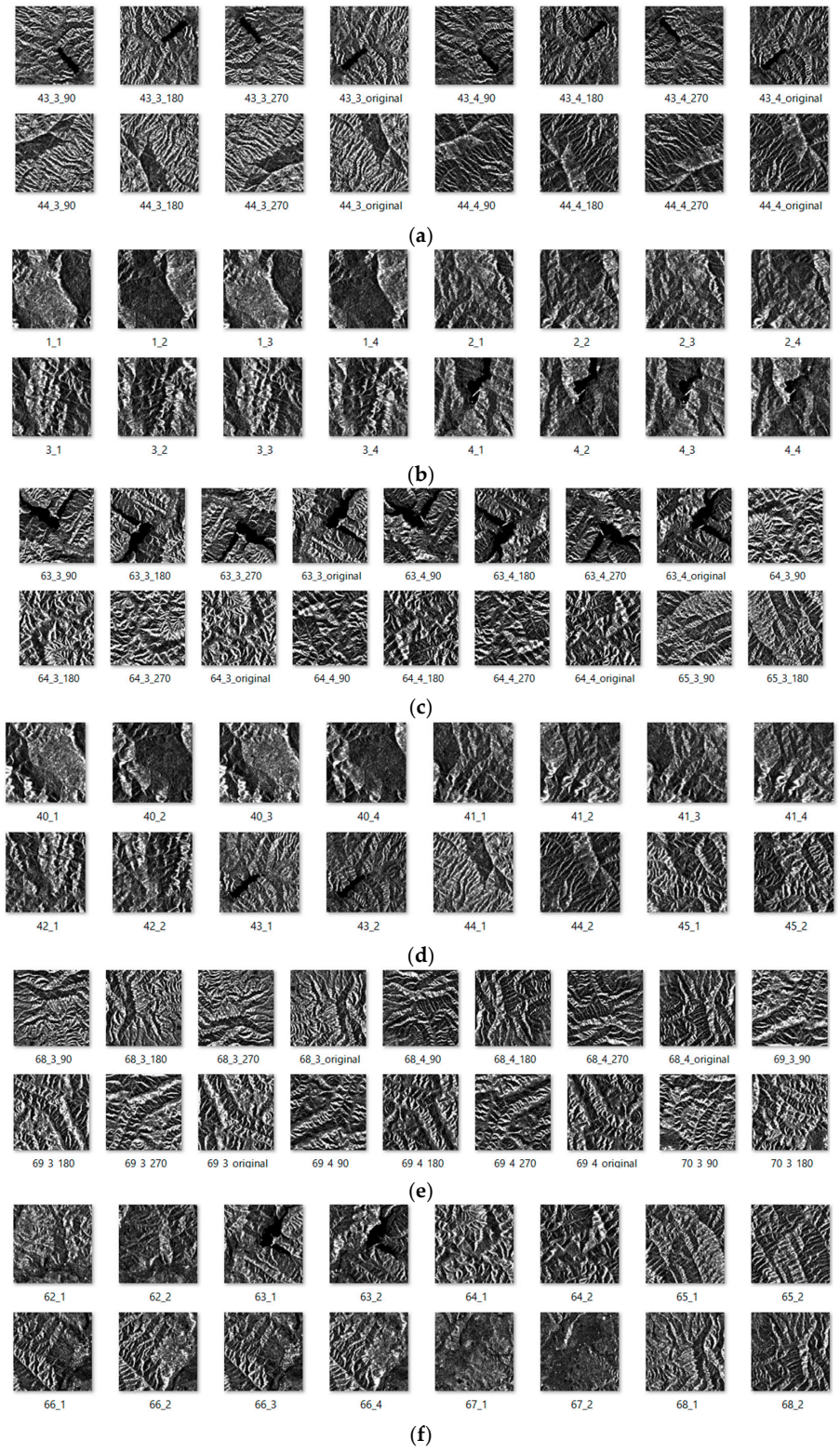


Figure 7. Small portions of training, validation, and test samples of the VV polarization of the imagery data for landslide areas and those for non-landslide areas. (**a**) A small portion of training samples from the VV polarization of the imagery data for landslide areas; (**b**) a small portion of training samples from the VV polarization of the imagery data for non-landslide areas; (**c**) a small portion of validation samples from the VV polarization of imagery data for landslide areas; (**d**) a small portion of validation samples from the VV polarization of the imagery data for non-landslide areas; (**e**) a small portion of test samples from the VV polarization of the imagery data for landslide areas; (**f**) a small portion of test samples from the VV polarization of the imagery data for non-landslide areas.

5.3. NDVI

The NDVI data derived from Sentinel-2/MSI are available via the EO-Browser platform. Figure 8 illustrates the NDVI for the Iburi, Atsuma region in Hokkaido:

(a) NDVI acquired on 5 September 2018 (pre-earthquake)
(b) NDVI acquired on 15 September 2018 (post-earthquake)

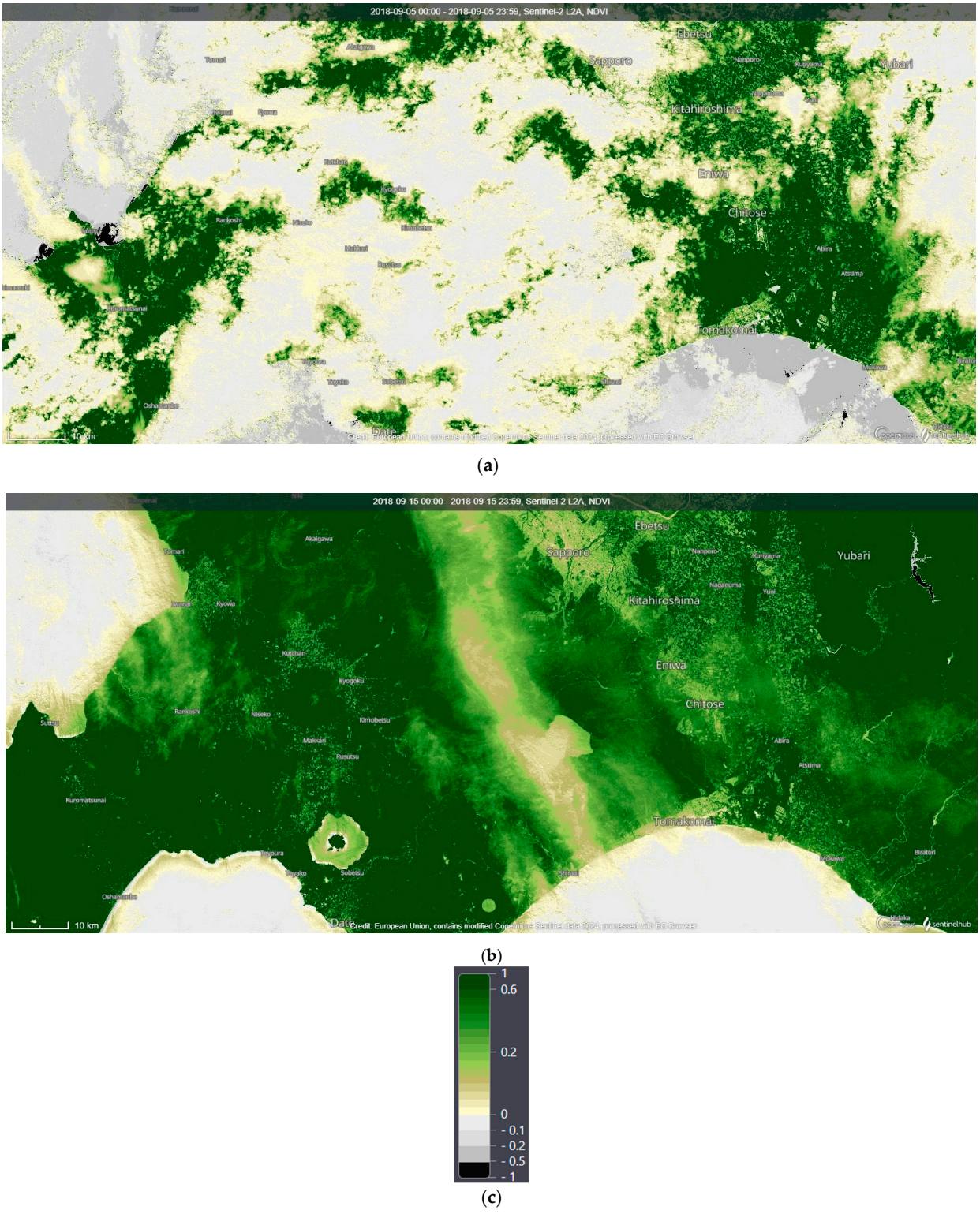


Figure 8. Sentinel-2/MSI NDVI data were acquired on 5 September 2018 (just before the earthquake) and on 15 September 2018 (after the earthquake). (**a**) 5 September 2018; (**b**) 15 September 2018; (**c**) Color Scale.

These images highlight the vegetation changes in the region before and after the earthquake.

As shown in Figure 8, Sentinel-2/MSI NDVI data often include cloudy conditions as the revisit cycle of the Sentinel-2 satellite is 10 days. This allows the NDVI data to be acquired approximately every 10 days.

The NDVI in landslide-affected areas, as observed on 15 September 2018, is lower compared to that on 5 September 2018. This decrease in the NDVI is attributed to the removal of vegetation caused by the earthquake, leading to a visible change in land cover from vegetation to bare ground.

5.4. Classification Performance

The results of landslide classification using EfficientNetV2 with VV, VH, and RVI images (unconverted) for the Hokkaido earthquake are presented. VV and VH backscatter signals show landslide areas as whitish, while the RVI clearly indicates disaster areas as black. Although VV and VH are challenging to distinguish from objects at different angles, this experiment highlights that the RVI is particularly effective for identifying landslides in mountainous regions. It is obvious that the classification performance with the RVI images is superior to those with VV and VH because the RVI can be calculated with the VV and VH polarization of the data, and vegetated or non-vegetated areas are hard to identify using only single VV or single VH polarizations of data due to the scattering behavior of vegetations (single or plural scattering).

Data from Hokkaido were collected, yielding 364 pairs for testing after 200 epochs of training. In addition to the data from 20180820, 20180824, 20180913, and 20180917, and data from 20180925 and 20180929 were also included. The value 20180925 represents the ascending pass, while 20180929 is the descending pass. The results were obtained with a learning rate of 0.000005 over 50 epochs. The batch sizes were set to 16 for training, 8 for validation, and 1 for testing. In this case, a label of 0 indicates a non-disaster area, while 1 represents a disaster area (opposite to the previous description). The dataset was augmented by rotating and amplifying:

An amount of 148 images of non-disaster areas for training.

An amount of 96 images of disaster areas for training.

An amount of 48 images of non-disaster areas for validation.

An amount of 32 images of disaster areas for validation.

An amount of 48 images of non-disaster areas for testing.

An amount of 28 images of disaster areas for testing.

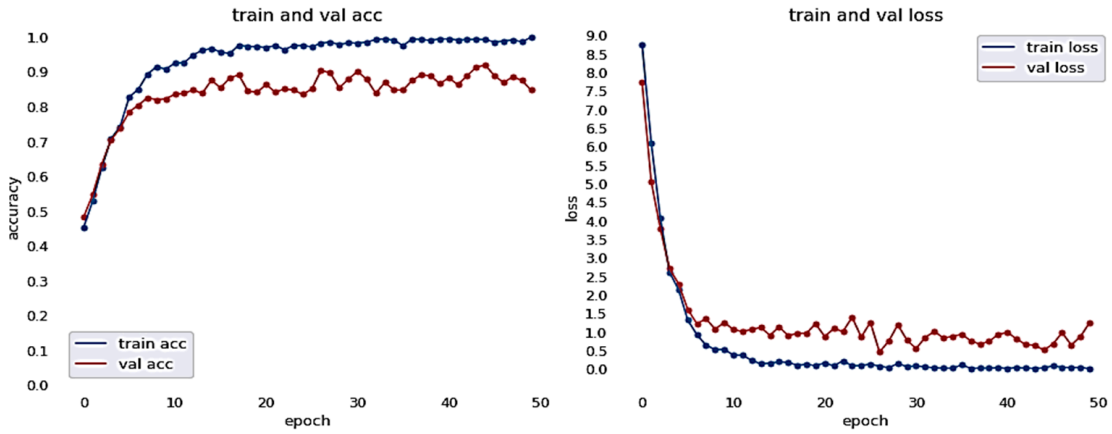
In total, the training set included 592 images of non-disaster areas and 384 images of disaster areas, while the validation set had 192 images of non-disaster areas and 128 images of disaster areas. The test set comprised 192 images of non-disaster areas and 112 images of disaster areas.

Classification performance was evaluated using EfficientNetV2 through learning processes, confusion matrices, and ROC curves for the following cases:

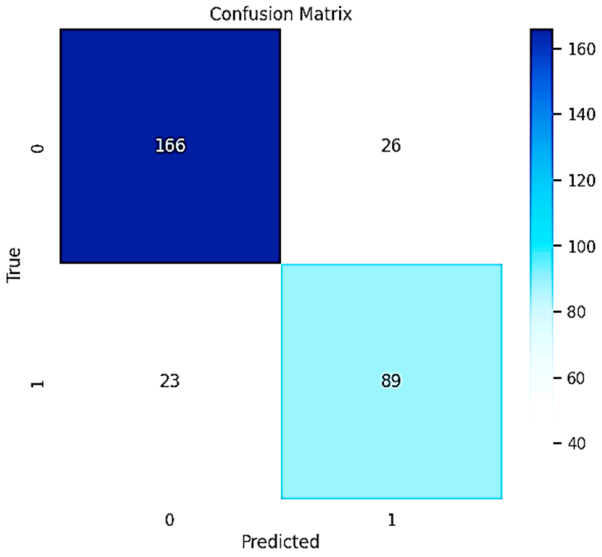
RVI only—Figure 9a–c

VH polarization only—Figure 9d–f

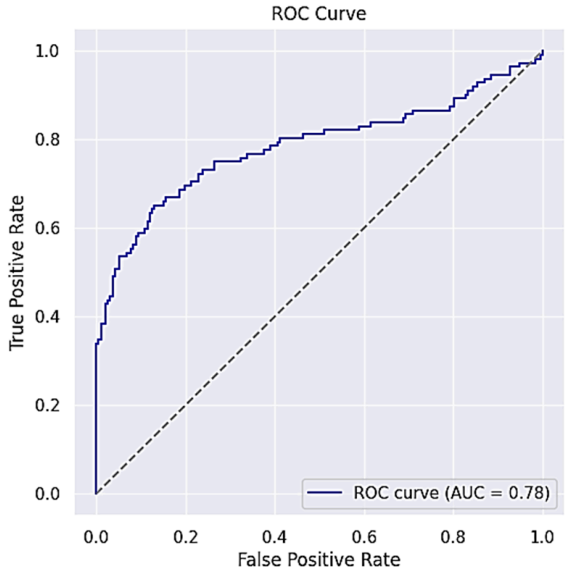
VV polarization only—Figure 9g–i



(**a**)

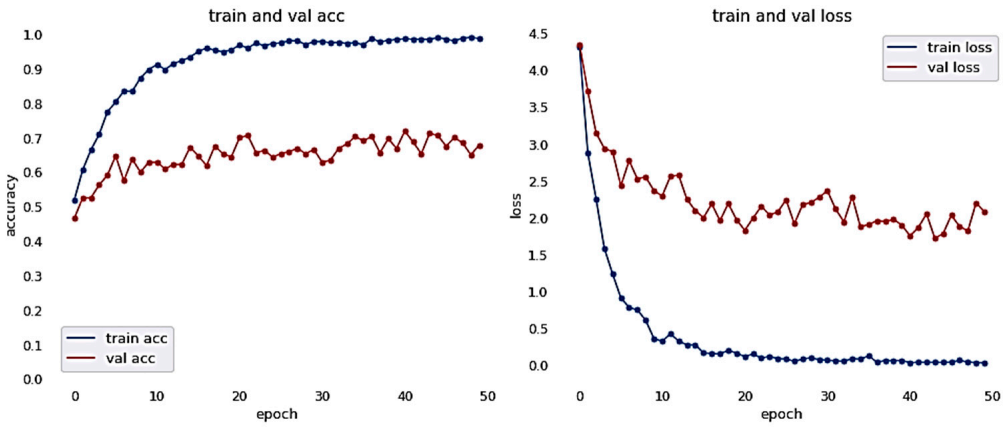


(**b**)

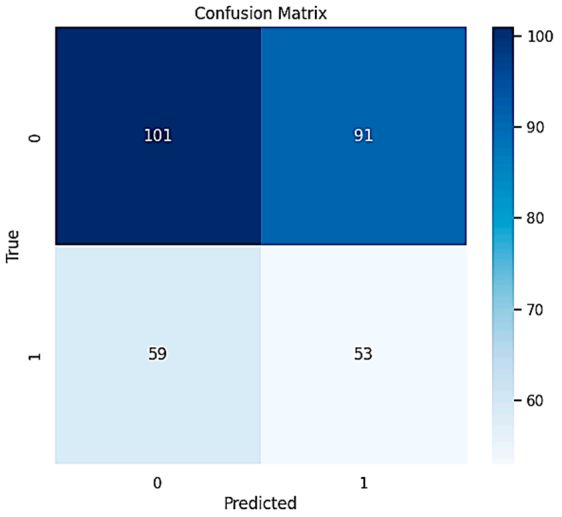


(**c**)

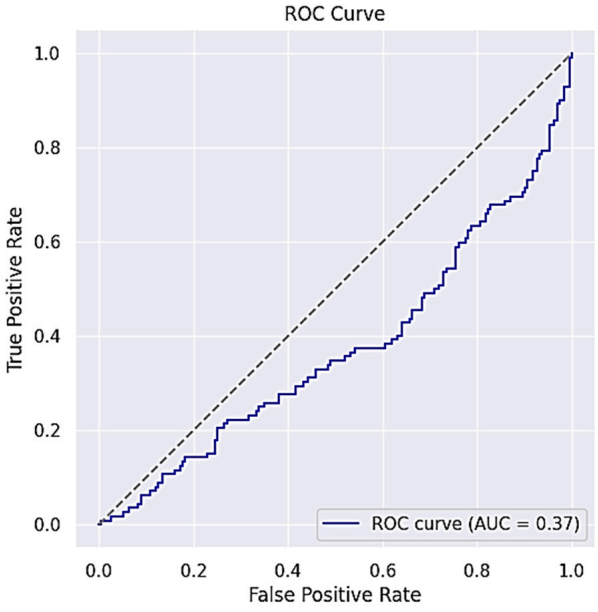
Figure 9. *Cont.*



(**d**)

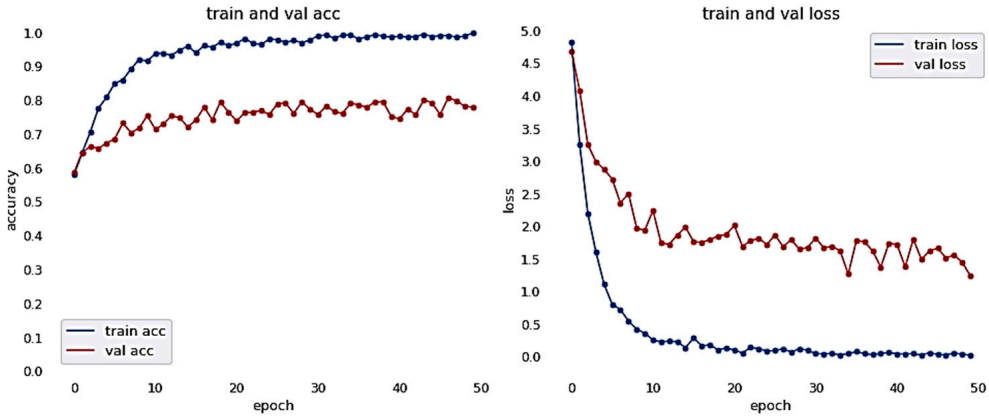


(**e**)

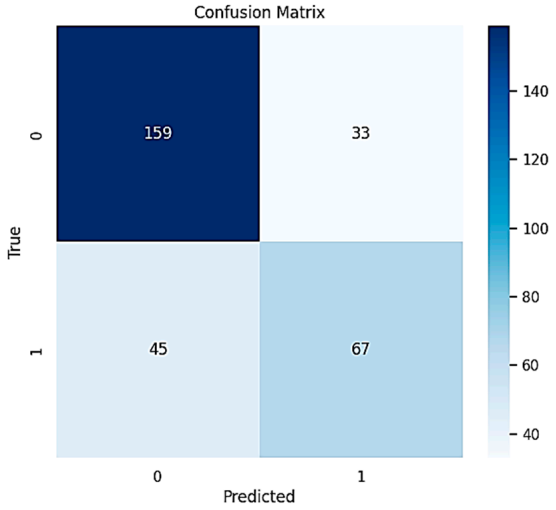


(**f**)

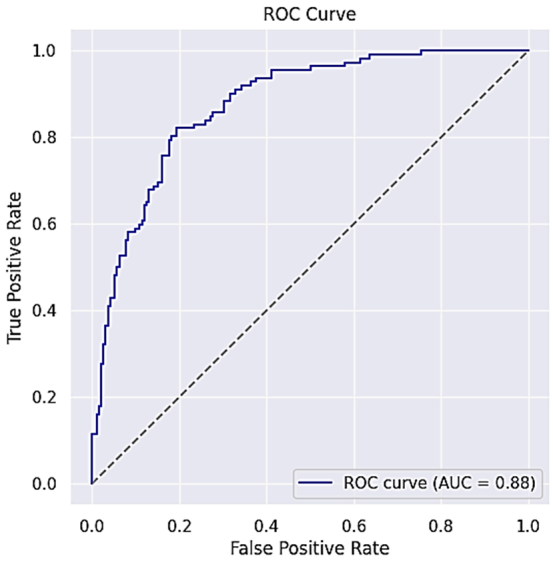
Figure 9. *Cont.*



(**g**)



(**h**)



(**i**)

Figure 9. Classification performances of EfficientNetV2 for the landslide area or not in cases of using RVI, VH polarization, and VV polarization data used. (**a**) Case (1): RVI; (**b**) Case (1): RVI; (**c**) Case (1): RVI; (**d**) Case (2): VH polarization only; (**e**) Case (2): VH polarization only; (**f**) Case (2): VH polarization only; (**g**) Case (3): VV polarization only; (**h**) Case (3): VV polarization only; (**i**) Case (3): VV polarization only.

In these cases, the class label "0" represents the landslide area, while "1" indicates a non-landslide area.

It is found that the Percent of Correct Classification PCC in case (1) (using RVI data) is 83.9% while that of case (2) (VH polarization data) is 50.7% and that of case (3) (VV polarization data) is 74.3%.

6. Discussions

The results from the PCC (Pearson Correlation Coefficient) indicate that the classification using the RVI data yields a performance improvement of 65.5% compared to using VH polarization data and 12.9% better than using VV polarization data. Additionally, the Area Under the Curve (AUC) for the RVI data are 0.78, while for VH polarization data, it is 0.34, and for VV polarization data, it is 0.88. This means that the AUC using RVI data are 129.4% better than using VH polarization data, and 11.4% less than using VV polarization data. These results show that RVI data provides significantly superior classification performance compared to both VH and VV polarization data.

One key reason for the enhanced performance of the RVI-based method is that RVI combines information from both VV and VH polarization data, capturing aspects of multiple scattering and single scattering mechanisms. In contrast, VV and VH data separately reflect only multiple scattering and single scattering components, respectively. This comprehensive information provided by the RVI allows for more accurate detection and classification of landslide areas.

7. Conclusions

A method utilizing the radar vegetation index (RVI) derived from Sentinel-1/SAR data for non-vegetated area detection is proposed. Additionally, the learning performance of EfficientNetV2 for classifying landslide areas using the RVI, along with VV and VH polarizations from Sentinel-1/SAR data, is evaluated. The classification performances of these datasets—RVI, VV, and VH—are compared to determine their effectiveness.

Through experiments conducted with Sentinel-1/SAR data from the Iburi district in Hokkaido, Japan, where a severe earthquake occurred in 2018, it is evident that the classification performance using RVI derived from VV and VH polarization data outperforms the other methods. The Pearson Correlation Coefficient (PCC) results indicate that using RVI data are 65.5% better than using VH polarization data and 12.9% better than using VV polarization data.

The Area Under the Curve (AUC) metric further demonstrates this advantage. The AUC for the RVI data is 0.78, while for VH polarization data, it is 0.34, and for VV polarization data, it is 0.88. This means the AUC using RVI data are 129.4% better than VH polarization data and 11.4% less than VV polarization data. These results clearly show that the RVI-derived data provides a significantly superior classification performance compared to both VH and VV polarization data.

In conclusion, the utilization of the RVI data from Sentinel-1/SAR, combined with EfficientNetV2, offers a highly effective approach for detecting landslide areas, outperforming classification methods based solely on VV and VH polarizations.

8. Future Research Works

Currently, this method is primarily applied to data from mountainous regions. However, in the future, we plan to expand the study to assess the classification accuracy of the RVI for landslide detection in urban areas, coastal regions, and other diverse environments. Additionally, as only basic processing has been performed so far, normalization techniques will be applied to further examine the impact on classification accuracy.

Furthermore, since the RVI data includes information for areas affected by smaller disasters, it is expected that narrowing the dataset could enhance accuracy. Therefore, we will verify classification accuracy by considering the size of the disaster-affected areas.

Author Contributions: Methodology, K.A.; Software, Y.N.; Resources, H.O. All authors have read and agreed to the published version of the manuscript.

Funding: This research received no external funding.

Data Availability Statement: The original contributions presented in this study are included in the article. Further inquiries can be directed to the corresponding author.

Conflicts of Interest: The authors declare no conflict of interest.

References

1. Nasirzadehdizaji, R.; Balik Sanli, F.; Abdikan, S.; Cakir, Z.; Sekertekin, A.; Ustuner, M. Sensitivity Analysis of Multi-Temporal Sentinel-1 SAR Parameters to Crop Height and Canopy Coverage. *Appl. Sci.* **2019**, *9*, 655. [CrossRef]
2. Forum of ESA. Available online: https://forum.step.esa.int/t/creating-radar-vegetation-index/12444/18 (accessed on 6 December 2024).
3. Mandal, D. Radar Vegetation Index for Sentinel-1 (RVI4S1) Script. Custom Scripts Sentinel-Hub. 2022. Available online: https://www.sentinel-hub.com/develop/community/past-contests/ (accessed on 15 January 2025).
4. Copernicus Data Space Ecosystem, Calculate Radar Vegetation Index (RVI) Using Sentinel-1 GRD Collection. Available online: https://documentation.dataspace.copernicus.eu/APIs/openEO/openeo-community-examples/python/RVI/RVI.html (accessed on 6 December 2024).
5. Hu, X.; Li, L.; Huang, J.; Zeng, Y.; Zhang, S.; Su, Y.; Hong, Y.; Hong, Z. Radar vegetation indices for monitoring surface vegetation: Developments, challenges, and trends. *Sci. Total Environ.* **2024**, *945*, 173974. [CrossRef]
6. Mandal, D.; Bhattacharya, A.; Rao, Y. Radar Vegetation Indices for Crop Growth Monitoring. In *Radar Remote Sensing for Crop Biophysical Parameter Estimation*; Springer: Singapore, 2021. [CrossRef]
7. Mandal, D.; Ratha, D.; Bhattacharya, A.; Kumar, V.; Mcnairn, H.; Rao, Y.S.; Frery, A. A Radar Vegetation Index for Crop Monitoring Using Compact Polarimetric SAR Data. *IEEE Trans. Geosci. Remote Sens.* **2020**, *58*, 6321–6335. [CrossRef]
8. Thenkabail, P.S.; Lyon, J.G.; Huete, A. *Hyperspectral Remote Sensing of Vegetation*, 2nd ed.; Four Volume Set; CRC Press: Boca Raton, FL, USA, 2019; ISBN 9781315159287.
9. Wang, B.; Liu, Y.; Sheng, Q.; Li, J.; Wang, S.; Qiao, Y.; He, H. Exploring the effects of crop growth differences on radar vegetation index response and crop height estimation using dynamic monitoring model. ISPRS Ann. Photogramm. *Remote Sens. Spat. Inf. Sci.* **2024**, *X-1-2024*, 225–232. [CrossRef]
10. Chang, J.G.; Shoshany, M.; Oh, Y. Polarimetric Radar Vegetation Index for Biomass Estimation in Desert Fringe Ecosystems. *IEEE Trans. Geosci. Remote Sens.* **2018**, *56*, 7102–7108. [CrossRef]
11. Mandal, D.; Kumar, V.; Ratha, D.; Dey, S.; Bhattacharya, A.; Lopez-Sanchez, J.M.; McNairn, H.; Rao, Y.S. Dual polarimetric radar vegetation index for crop growth monitoring using sentinel-1 SAR data. *Remote Sens. Environ.* **2020**, *247*, 111954. [CrossRef]
12. Bhogapurapu, N.; Dey, S.; Mandal, D.; Bhattacharya, A.; Karthikeyan, L.; McNairn, H.; Rao, Y.S. Soil moisture retrieval over croplands using dual-pol L-band GRD SAR data. *Remote Sens. Environ.* **2022**, *271*, 112900. [CrossRef]
13. dos Santos, E.P.; da Silva, D.D.; do Amaral, C.H. Vegetation cover monitoring in tropical regions using SAR-C dual-polarization index: Seasonal and spatial influences. *Int. J. Remote Sens.* **2021**, *42*, 7581–7609. [CrossRef]
14. Bhogapurapu, N.; Dey, S.; Bhattacharya, A.; Mandal, D.; Lopez-Sanchez, J.M.; McNairn, H.; López-Martínez, C.; Rao, Y.S.S. Dual-polarimetric descriptors from Sentinel-1 GRD SAR data for crop growth assessment. *ISPRS J. Photogramm. Remote Sens.* **2021**, *178*, 20–35. [CrossRef]
15. dos Santos, E.P. A Python and R Blend for Processing Sentinel-1 Images, Getting SAR-Based Vegetation Indices, and Sampling Raster. Available online: https://eupassarinho.github.io/sentinel-1-SAR-vegetation-indices/ (accessed on 6 December 2024).
16. Villarroya-Carpio, A.; Lopez-Sanchez, J.M.; Engdahl, M.E. Sentinel-1 interferometric coherence as a vegetation index for agriculture. *Remote Sens. Environ.* **2022**, *280*, 113208. [CrossRef]
17. Flores, A.; Herndon, K.; Thapa, R.; Cherrington, E. (Eds.) *Comprehensive Methodologies for Forest Monitoring and Biomass Estimation*; NASA: Washington, DC, USA, 2019. [CrossRef]
18. Xu, Q.; Zhao, B.; Dai, K.; Dong, X.; Li, W.; Zhu, X.; Yang, Y.; Xiao, X.; Wang, X.; Huang, J.; et al. Remote sensing for landslide investigations: A progress report from China. *Eng. Geol.* **2023**, *321*, 107156. [CrossRef]
19. Cheng, G.; Wang, Z.; Huang, C.; Yang, Y.; Hu, J.; Yan, X.; Tan, Y.; Liao, L.; Zhou, X.; Li, Y.; et al. Advances in Deep Learning Recognition of Landslides Based on Remote Sensing Images. *Remote. Sens.* **2024**, *16*, 1787. [CrossRef]

20. Rosi, A.; Vannocci, P.; Tofani, V.; Gigli, G.; Casagli, N. Landslide Characterization Using Satellite Interferometry (PSI), Geotechnical Investigations and Numerical Modelling: The Case Study of Ricasoli Village (Italy). *Int. J. Geosci.* **2013**, *4*, 904–918. [CrossRef]
21. Akinci, H.; Kilicoglu, C.; Dogan, S. Random Forest-Based Landslide Susceptibility Mapping in Coastal Regions of Artvin, Turkey. *ISPRS Int. J. Geo-Inf.* **2020**, *9*, 553. [CrossRef]
22. Amatya, P.; Kirschbaum, D.; Stanley, T.; Tanyas, H. Landslide mapping using object-based image analysis and open source tools. *Eng. Geol.* **2021**, *282*, 106000. [CrossRef]
23. Bekaert, D.P.S.; Handwerger, A.; Agram, P.; Kirschbaum, D.B. InSAR-based detection method for mapping and monitoring slow-moving landslides in remote regions with steep and mountainous terrain: An application to Nepal. *Remote Sens. Environ.* **2020**, *249*, 111983. [CrossRef]
24. Mondini, A.C.; Santangelo, M.; Rocchetti, M.; Rossetto, E.; Manconi, A.; Monserrat, O. Sentinel-1 SAR Amplitude Imagery for Rapid Landslide Detection. *Remote. Sens.* **2019**, *11*, 760. [CrossRef]
25. Froude, M.J.; Petley, D.N. Global fatal landslide occurrence from 2004 to 2016. *Nat. Hazards Earth Syst. Sci.* **2018**, *18*, 2161–2181. [CrossRef]
26. Zhang, Q.; Wang, T. Deep Learning for Exploring Landslides with Remote Sensing and Geo-Environmental Data: Frameworks, Progress, Challenges, and Opportunities. *Remote. Sens.* **2024**, *16*, 1344. [CrossRef]
27. Zhao, C.; Lu, Z. Remote Sensing of Landslides—A Review. *Remote. Sens.* **2018**, *10*, 279. [CrossRef]

Disclaimer/Publisher's Note: The statements, opinions and data contained in all publications are solely those of the individual author(s) and contributor(s) and not of MDPI and/or the editor(s). MDPI and/or the editor(s) disclaim responsibility for any injury to people or property resulting from any ideas, methods, instructions or products referred to in the content.